



Objective Lagrangian Vortex Cores and their Visual Representations

Tobias Günther , and Holger Theisel 

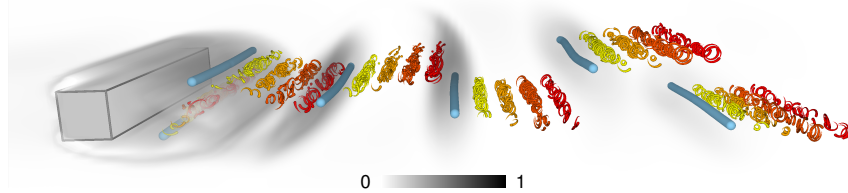


Fig. 1: We propose a novel objective vortex coreline extraction method, which optimizes the reference frame of observers that are for the first time guaranteed to follow along pathlines, i.e., they are guaranteed to be Lagrangian. Vortex cores arise as minima (in 2D) and valley lines (in 3D) of an observed time derivative. Here, the vortex corelines and their paths are visualized for the SQUARE CYLINDER flow. To show the swirling motion, we release streamlines (color-coded by time from yellow to red) in subsequent time steps in the observed vector field, which demonstrates the rotating motion. The volume rendering displays the vortex deviation error scalar field.

Abstract—The numerical extraction of vortex cores from time-dependent fluid flow attracted much attention over the past decades. A commonly agreed upon vortex definition remained elusive since a proper vortex core needs to satisfy two hard constraints: it must be objective and Lagrangian. Recent methods on objectivization met the first but not the second constraint, since there was no formal guarantee that the resulting vortex coreline is indeed a pathline of the fluid flow. In this paper, we propose the first vortex core definition that is both objective and Lagrangian. Our approach restricts observer motions to follow along pathlines, which reduces the degrees of freedoms: we only need to optimize for an observer rotation that makes the observed flow as steady as possible. This optimization succeeds along Lagrangian vortex corelines and will result in a non-zero time-partial everywhere else. By performing this optimization at each point of a spatial grid, we obtain a residual scalar field, which we call vortex deviation error. The local minima on the grid serve as seed points for a gradient descent optimization that delivers sub-voxel accurate corelines. The visualization of both 2D and 3D vortex cores is based on the separation of the movement of the vortex core and the swirling flow behavior around it. While the vortex core is represented by a pathline, the swirling motion around it is visualized by streamlines in the correct frame. We demonstrate the utility of the approach on several 2D and 3D time-dependent vector fields.

Index Terms—Flow visualization, vortices, objective methods

1 INTRODUCTION

Vortices and in particular vortex cores are among the most interesting and relevant features in fluid flows. Vortex cores have a simple common understanding: the flow swirls/revolves around a point (in 2D) or an axis line (in 3D) [16]. This point/axis line is called vortex core. Vortex cores may move over time. Vortex corelines in 3D may also change their shape, split, merge, appear, and disappear over time. Despite this common understanding, there is no commonly accepted unique definition of vortex cores. There are, however, a few commonly accepted desired properties of vortex cores and topological features [4]:

- **Lagrangian.** In 2D, vortex cores are pathlines of the flow. In 3D, vortex cores are curves advected by the flow, i.e., path surfaces.
- **Objectivity.** An arbitrarily moving observer should always observe the same vortex core, independent of its own movement.

Existing approaches to extract and visualize vortex cores do not meet both properties. Recently, Rautek et al. [33] introduced a new approach to track 2D vortex cores by applying a joint optimization in the flow domain and in the space of all Killing fields describing the observer motion. The resulting objective moving vortex cores are compared with existing approaches, such as the approach by Günther et al. [14]. Numerical tests on several data sets revealed comparable results. Further, [33] claimed that the resulting vortex cores are pathlines, where

- Tobias Günther, FAU Erlangen-Nürnberg. E-mail: tobias.guenther@fau.de
- Holger Theisel, University of Magdeburg E-mail: theisel@ovgu.de.

Manuscript received xx xxx. 201x; accepted xx xxx. 201x. Date of Publication xx xxx. 201x; date of current version xx xxx. 201x. For information on obtaining reprints of this article, please send e-mail to: reprints@ieee.org. Digital Object Identifier: xx.xxx/TVCG.201x.xxxxxxx

deviations from perfect pathlines are only due to numerical inaccuracies. For visual representation, a magic lens metaphor was introduced, allowing to show both the swirling flow around the center and the movement of the center separately by a LIC visualization [5] and a 3D space-time metaphor. In this paper, we make the following contributions:

- We give a theoretical comparison of the vortex cores in [33] with existing approaches, in particular with the vortex cores in [14]. With this we theoretically confirm the similarity of [33] and [14] for vortex cores shown by numerical experiments in [33].
- We show that the claim of [33], which states that their vortex cores are in general pathlines, is not correct. This leads to the statement that none of the existing approaches for vortex core tracking is guaranteed to give corelines that are perfect pathlines.
- We introduce a new approach to compute vortex cores that are guaranteed to be pathlines/path surfaces. The main idea of our approach is to consider all pathlines as potential vortex cores. Instead of searching among all moving reference frames, we only consider those that reproduce pathlines as vortex cores. The result is the definition of a vortex deviation error (VDE) that indicates for each pathline how suitable it acts as a vortex core.
- We show that the computation of VDE for a pathline is equivalent to solving an Euler-Lagrange equation. We further show that after a proper discretization, this can be computed by solving a sparse linear system with a guaranteed unique solution.
- We introduce a new visual representation for moving vortex cores that is based on a separate representation of the swirling behavior and the moving core. For this, we used a careful combination of streamlines, pathlines, and extremal lines. Contrary to existing work [33], our representation is applicable in both 2D and 3D.

1.1 Notation and basic properties

Formally, we denote a (2D or 3D) time-dependent velocity field as $\mathbf{v}(\mathbf{x}, t) = (u(x, y, [z,]t), v(x, y, [z,]t), [w(x, y, z, t)])^T$ where the terms in square brackets $[]$ appear only in 3D. Further, let

$$\nabla \mathbf{v}(\mathbf{x}, t) = \mathbf{J}(\mathbf{x}, t) = \begin{pmatrix} u_x & u_y & [u_z] \\ v_x & v_y & [v_z] \\ [w_x] & [w_y] & [w_z] \end{pmatrix}, \quad \mathbf{v}_t(\mathbf{x}, t) = \frac{\partial \mathbf{v}}{\partial t} \quad (1)$$

be the Jacobian and the time derivative of \mathbf{v} , respectively. Let

$$\dot{\mathbf{v}} = \mathbf{J}\mathbf{v} + \mathbf{v}_t, \quad \dot{\mathbf{J}} = \begin{pmatrix} \dot{u}_x & \dot{u}_y & [\dot{u}_z] \\ \dot{v}_x & \dot{v}_y & [\dot{v}_z] \\ [\dot{w}_x] & [\dot{w}_y] & [\dot{w}_z] \end{pmatrix} = \left(\frac{\partial \mathbf{J}}{\partial x}, \frac{\partial \mathbf{J}}{\partial y}, \left[\frac{\partial \mathbf{J}}{\partial z} \right] \right) \mathbf{v} + \frac{\partial \mathbf{J}}{\partial t} \quad (2)$$

be the material derivatives of the velocity and the Jacobian, respectively. In 3D, we denote the vorticity vector of \mathbf{v} as

$$\boldsymbol{\omega}_{\mathbf{v}} = (w_y - v_z, u_z - w_x, v_x - u_y)^T. \quad (3)$$

We use the matrix operator \mathbf{A} with the following function: in 2D, it maps a scalar into an antisymmetric matrix ($\mathbb{R} \rightarrow \mathbb{R}^{2 \times 2}$), and in 3D it maps a vector into an antisymmetric matrix ($\mathbb{R}^3 \rightarrow \mathbb{R}^{3 \times 3}$) by

$$\mathbf{A}(\alpha) = \begin{pmatrix} 0 & -\alpha \\ \alpha & 0 \end{pmatrix}, \quad \mathbf{A}((\alpha, \beta, \gamma)^T) = \begin{pmatrix} 0 & -\gamma & \beta \\ \gamma & 0 & -\alpha \\ -\beta & \alpha & 0 \end{pmatrix}. \quad (4)$$

In particular, in 2D we introduce the rotation matrix

$$\mathbf{Q} = \mathbf{A}(-1) = \begin{pmatrix} 0 & 1 \\ -1 & 0 \end{pmatrix}. \quad (5)$$

Following [20], we describe a moving reference frame as Killing field

$$\mathbf{w}(\mathbf{x}, t) = \mathbf{t} + \mathbf{A}(\boldsymbol{\omega}) \cdot \mathbf{x} \quad (6)$$

where $\mathbf{t} = \mathbf{t}(t)$ is a time-dependent translation vector and $\boldsymbol{\omega} = \boldsymbol{\omega}(t)$ is the time-dependent vorticity of \mathbf{w} . Note that $\mathbf{w}(\mathbf{x}, t)$ is a Killing field since $\nabla \mathbf{w}(\mathbf{x}, t) + \nabla \mathbf{w}(\mathbf{x}, t)^T = \mathbf{0}$. Note that $\boldsymbol{\omega}$ is a scalar in 2D but a 3-vector $\boldsymbol{\omega} = (\omega_x, \omega_y, \omega_z)^T$ in 3D. This means that a Killing field (6) in 2D has 3 degrees of freedom (the 2-vector \mathbf{t} and the scalar $\boldsymbol{\omega}$), but in 3D it has 6 degrees of freedom (the 3-vector \mathbf{t} and the 3-vector $\boldsymbol{\omega}$) [40].

2 RELATED WORK

Vortex extraction is an active area of research [16]. Conceptually, there are two analysis goals: scientists are either interested in the geometric extent of a vortex, for which *region-based* methods are used, or they care about the exact centerline around which fluid parcels are rotating, for which *line-based* methods are used. The following section gives a coarse overview of the recent developments. For a comprehensive discussion, we refer to the survey of Günther and Theisel [16].

2.1 Region-based Vortex Extraction

Region-based methods commonly calculate scalar fields that are thresholded appropriately to define regions with vortical behavior. Early and common scalar fields are the imaginary part of the Jacobian's eigenvalues [7, 41], the vorticity value [27], the Q -criterion [23], and the λ_2 criterion [24]. More recently, objectivity shifted into focus. Haller et al.'s M_z criterion [21], as well as the instantaneous and Lagrangian averaged vorticity deviation [22] are recent examples.

2.2 Line-based Vortex Extraction

The first line-based methods have been developed for steady flows, including the tracing of separatrices from swirling saddles in 3D flow [13] and the predictor-corrector extraction of pressure valley lines [3]. Sudaji and Haines [37] characterized vortex corelines as lines along which the flow vector aligns with the single eigenvector whose eigenvalue is not complex. Peikert and Roth [30] generalized this concept

by the parallel vectors operator, for which this was one among many applications. Apart from generalizations of the expected shape to bent corelines [35], several directions have been followed to extend the concept to time-dependent flow [11, 39]. At that time, approaches reached Galilean invariance [39] or rotation invariance [15].

2.3 Objectivization Methods

The growing interest in objective [21] feature extraction methods, was founded on the observation that in time-dependent flow the motion of reference frames and features is relative to each other. Thus, formerly proving that a feature definition is invariant to observer motions entails that the feature definition is able to successfully detect moving features. The invariance class called *objectivity* is able to describe temporally smooth rotations and translations of the observer [38]. Several directions have been explored to make existing feature definitions objective, which included the observation of the spin tensor in the objective eigenvector basis of the strain-rate tensor [1, 9], the substitution of the spin tensor by the spin deviation tensor [22, 28], and the search for reference frames in which the observed vector field becomes steady [14]. The latter has its roots in early theoretical considerations of vortices being apparent as swirling streamlines in appropriately chosen reference frames [29, 34], for which Günther et al. [14] proposed a first numerical algorithm. Since then, several extensions have been proposed that widened the invariance classes [2, 18], considered higher dimensions [17], or operated on sets of few trajectories [10]. A notable step forward was the characterization of observer motions as Killing fields [20], which paved the path to the treatment of curved manifolds [32], and new lens-based exploration tools [33].

2.4 Vortex Cores as Pathlines

The concept of considering vortex corelines as pathlines goes back to the early 90's when many formal vortex definitions were laid out. We follow the definition of Robinson [34], who stated "A vortex exists when instantaneous streamlines mapped onto a plane normal to the vortex core exhibit a roughly circular or spiral pattern, when viewed from a reference frame moving with the center of the vortex core." Even though this understanding allows various definitions (i.e., choices of the vortex core), it demands that the (unknown) vortex core is a path line (in 2D). This can be seen by the following argumentation for the 2D case: Given is a velocity field $\mathbf{v}(\mathbf{x}, t)$ and an unknown differentiable curve $\mathbf{c}(t)$ acting as a vortex core. Further let $\mathbf{c}_t(t) = d\mathbf{c}(t)/dt$ be its first derivative, i.e., its tangent. We observe \mathbf{v} under a reference frame moving with the vortex core. This reference frame is described by a Killing field $\mathbf{w}(\mathbf{x}, t)$ that is tangential to the vortex coreline, i.e.:

$$\mathbf{w}(\mathbf{c}(t), t) = \mathbf{c}_t(t). \quad (7)$$

Concerning [34], the observed velocity field $\mathbf{v} - \mathbf{w}$ exhibits a circular or spiral pattern, i.e., it vanishes at the core itself:

$$(\mathbf{v} - \mathbf{w})(\mathbf{c}(t), t) = \mathbf{v}(\mathbf{c}(t), t) - \mathbf{w}(\mathbf{c}(t), t) = \mathbf{0} \quad (8)$$

Rearranging for $\mathbf{w}(\mathbf{c}(t), t)$ and inserting this in Eq. (7) gives

$$\mathbf{v}(\mathbf{c}(t), t) = \mathbf{c}_t(t), \quad (9)$$

meaning that $\mathbf{c}(t)$ is a path line. In 3D, a moving vortex core line can be described as a parametric surface $\mathbf{c}(s, t)$ where s is the parametrization of the core line at a time t . This means that considering $t = t_0 = \text{const}$ describes the vortex core $\mathbf{c}(s, t_0)$ as a parametric curve in s at the time t_0 . The projection of the observed velocity into the plane normal to the vortex core is $(\mathbf{v} - \mathbf{w})(\mathbf{c}(s, t), t) - k \cdot \mathbf{c}_s(s, t)$ with $k = ((\mathbf{v} - \mathbf{w})^T \mathbf{c}_s) / ((\mathbf{c}_s)^T \mathbf{c}_s)$. Then, the observation of circular or spiral patterns in the projection perpendicular to the vortex core gives

$$(\mathbf{v} - \mathbf{w})(\mathbf{c}(s, t), t) - k \cdot \mathbf{c}_s(s, t) = \mathbf{0} \quad (10)$$

Inserting Eq. (7) into Eq. (10) gives

$$\mathbf{v}(\mathbf{c}(s, t), t) - \mathbf{c}_t(s, t) - k \cdot \mathbf{c}_s(s, t) = \mathbf{0} \quad (11)$$

which means that $\mathbf{c}(s,t)$ is a path surface, since $\mathbf{v}(\mathbf{c}(s,t),t)$ is a linear combination of the surface tangents $\mathbf{c}_t(s,t)$ and $\mathbf{c}_s(s,t)$. Existing definitions of vortex cores took this demand (vortex cores are path lines) as *soft constraint*. This means that extracted vortex cores are not path lines, but they were checked and filtered by their closeness to path lines. The papers considering the Lagrangian assumption as *soft constraint* include [2, 14, 18, 33, 39, 40]. Our paper is—to the best of our knowledge—the first approach to take the Lagrangian property as *hard constraint*: our vortex cores are perfect path lines.

3 COMPARISON OF EXISTING METHODS

Rautek et al. [33] introduced a new approach for the tracking of 2D vortex cores and compared it with existing approaches. While the comparison with standard methods like parallel vectors [35] gave superior results, the comparison with other advanced techniques [14] gave less unique results. Several test data sets reveal slightly better results for [33], others for [14]. Further, the difference of the results in [33] and [14] is rather small for all data sets. Rautek et al. [33] concluded that the new approach [33] can compete with [14].

For the sake of reproducibility and replicability, we conduct a new comparison of the vortex cores in [33] and [14]. Contrary to the comparison in [33], we do not run numerical tests on several data sets but we provide a theoretical comparison and analysis of [33] and [14]. (We consider other approaches [2, 18] as follow-up work of [14], and focus on the comparison of [33] and [14]).

Rautek et al. [33] and Günther et al. [14] follow a similar general idea: perform unsteadiness minimization under a dynamically moving area of interest in the flow domain. However, both approaches are formulated in different languages: [14] describes the unknown moving reference frame by a time-dependent rotation matrix and translation vector, while [33] represents it by a Killing vector field. Further [14] sets vortex cores as critical points of a vector field, while [33] applies a multi-parameter numerical minimization on a scalar field. Note that [33] applies a non-linear optimization in space and Killing-space, while our approach applies a linear optimization over the whole time-domain followed by a spatial non-linear optimization in space. To compare [14] with [33], we have to bring them first into a common formulation. Since [33] is defined in 2D only, we restrict the comparison to 2D.

3.1 Common setup

Given is a 2D velocity field \mathbf{v} that is observed under the (unknown) Killing field \mathbf{w} in Eq. (6) with translation $\mathbf{t} = (a(t), b(t))^T$. Both [14] and [33] consider the observed time derivative of \mathbf{v} under the moving reference system \mathbf{w} as [20]

$$\mathbf{m}(\mathbf{x}, \mathbf{a}, t) = \mathbf{v}_t - \mathbf{w}_t + \nabla \mathbf{v} \cdot \mathbf{w} - \nabla \mathbf{w} \cdot \mathbf{v} \quad (12)$$

with the unknown parameters (a, b, ω) and their derivatives in $\mathbf{a} = \mathbf{a}(t) = (a, b, \omega, \dot{a}, \dot{b}, \dot{\omega})^T$. This means that \mathbf{m} depends on the location (\mathbf{x}, t) , the parameters a, b, ω of the Killing field, and their time-derivatives $\dot{a}, \dot{b}, \dot{\omega}$. With \mathbf{a} we rewrite the Killing field \mathbf{w} in (6) as

$$\mathbf{w}(\mathbf{x}, \mathbf{a}, t) = \mathbf{W} \mathbf{a} \quad \text{with} \quad \mathbf{W} = \mathbf{W}(\mathbf{x}) = (\mathbf{I}, -\mathbf{Q}\mathbf{x}, \mathbf{0}, \mathbf{0}, \mathbf{0}) \quad (13)$$

where \mathbf{W} is a (2×6) matrix. Both [14] and [33] consider the (norm of the) observed time derivative not at a point \mathbf{x} but over a R -neighborhood $U_R(\mathbf{x})$ around \mathbf{x} at every point \mathbf{x} as

$$e_1 = e_1(\mathbf{x}, \mathbf{a}, t) = \frac{1}{A} \int_{U_R(\mathbf{x})} \mathbf{m}(\mathbf{y}, \mathbf{a}, t)^T \mathbf{m}(\mathbf{y}, \mathbf{a}, t) \, d\mathbf{y} \quad (14)$$

with $A = \text{area}(U_R(\mathbf{x}))$. Note that [33] uses the L_1 instead of the L_2 norm in Eq. (14). To make both approaches comparable, we assume the same norm for both. Here we choose the L_2 norm. Both [14] and [33] compute the minimizer of e_1 in \mathbf{a} :

$$\mathbf{a}_{opt} = \mathbf{a}_{opt}(\mathbf{x}, t) = \underset{\mathbf{a}}{\text{argmin}} \, e_1(\mathbf{x}, \mathbf{a}, t) \quad (15)$$

which gives an optimal Killing field \mathbf{w}_{opt} for every (\mathbf{x}, t) :

$$\mathbf{w}_{opt}(\mathbf{y}, \mathbf{x}, t) = \mathbf{W}(\mathbf{y}) \mathbf{a}_{opt}(\mathbf{x}, t). \quad (16)$$

Note that \mathbf{w}_{opt} describes not a single Killing field but a whole family. In fact, every point (\mathbf{x}, t) has its own optimal Killing field $\mathbf{w}_{opt}(\mathbf{y}, \mathbf{x}, t)$, i.e., $\nabla_{\mathbf{y}} \mathbf{w}_{opt}(\mathbf{y}, \mathbf{x}, t) + (\nabla_{\mathbf{y}} \mathbf{w}_{opt}(\mathbf{y}, \mathbf{x}, t))^T = \mathbf{0}$.

3.2 The differences of the approaches

Günther et al. [14] defined a moving vortex core $\mathbf{c}_{Gu}(t)$ as a tracked critical point of the vector field

$$\mathbf{g} = \mathbf{g}(\mathbf{x}, t) = \mathbf{v}(\mathbf{x}, t) - \mathbf{w}_{opt}(\mathbf{x}, \mathbf{x}, t), \quad (17)$$

i.e., the vortex core fulfills $\mathbf{g}(\mathbf{c}_{Gu}(t), t) = \mathbf{0}$. Contrary, Rautek et al. [33] introduced a second error function $e_2 = e_2(\mathbf{x}, \mathbf{a}, t) = (\mathbf{v} - \mathbf{w})^T (\mathbf{v} - \mathbf{w})$ and defined a moving vortex core $\mathbf{c}_{Ra}(t)$ as a local minimizer in both \mathbf{x} and \mathbf{a} of the final error function

$$e = e(\mathbf{x}, \mathbf{a}, t) = \mu e_1 + e_2 \quad (18)$$

for a certain positive weight μ . This means, the defining condition for a moving vortex core in [33] is

$$\frac{\partial e(\mathbf{c}_{Ra}(t), \mathbf{a}_{opt}(\mathbf{c}_{Ra}(t), t), t)}{\partial \mathbf{x}} = \mathbf{0}. \quad (19)$$

(To be precise, in [33] the optimization in \mathbf{a} is done by setting $\dot{a} = \dot{b} = \dot{\omega} = 0$ and searching for the optimal a, b, ω only, i.e., by ignoring the term \mathbf{w}_t in Eq. (12)).

3.3 Comparison

To compare the moving vortex cores $\mathbf{c}_{Gu}(t)$ [14] and $\mathbf{c}_{Ra}(t)$ [33], respectively, we get from the definition of $\mathbf{c}_{Gu}(t)$ above at the location $(\mathbf{c}_{Gu}(t), \mathbf{a}_{opt}(\mathbf{c}_{Gu}(t), t), t)$

$$\frac{\partial e_1}{\partial \mathbf{a}} = \frac{\partial e_2}{\partial \mathbf{x}} = \frac{\partial e_2}{\partial \mathbf{a}} = \mathbf{0}, \quad \frac{\partial e_1}{\partial \mathbf{x}} \neq \mathbf{0} \quad (20)$$

and in particular $e_2 = 0$. For $\mathbf{c}_{Ra}(t)$ at location $(\mathbf{c}_{Ra}(t), \mathbf{a}_{opt}(\mathbf{c}_{Ra}(t), t), t)$ we have by definition of a local minimum

$$\frac{\partial e}{\partial \mathbf{x}} = \mu \frac{\partial e_1}{\partial \mathbf{x}} + \frac{\partial e_2}{\partial \mathbf{x}} = \mathbf{0}, \quad \frac{\partial e}{\partial \mathbf{a}} = \mu \frac{\partial e_1}{\partial \mathbf{a}} + \frac{\partial e_2}{\partial \mathbf{a}} = \mathbf{0}. \quad (21)$$

This theoretical study shows that the locations of $\mathbf{c}_{Gu}(t)$ and $\mathbf{c}_{Ra}(t)$ are in general not the same. In practice, there are further differences. In [14], \mathbf{a}_{opt} is computed per grid point, and thus the critical point search in Eq. (17) interpolates between different observers, meaning that in $\frac{\partial e_2}{\partial \mathbf{x}}$ the e_2 uses a spatially (but smoothly) varying \mathbf{a} . In [33], \mathbf{a}_{opt} is constant in the critical point search, making \mathbf{w} a Killing field. However, [33] minimize (21) numerically with an ADMM algorithm, which ultimately favors one of the two terms. However, if \mathbf{a}_{opt} is constant within $U_R(\mathbf{x})$, both methods converge to each other for $\mu \rightarrow 0$ or for $e_1(\mathbf{c}_{Gu}(t), \mathbf{a}_{opt}(\mathbf{c}_{Gu}(t), t), t) \rightarrow 0$. If we assume the neighborhood $U_R(\mathbf{x})$ to be small enough to be covered by one reference frame, $e_1(\mathbf{c}_{Gu}(t), \mathbf{a}_{opt}(\mathbf{c}_{Gu}(t), t), t)$ is expected to be close to 0. This gives that in practice [14] and [33] give similar vortex cores. In particular, they exactly coincide if \mathbf{v} can be described as observation of a steady vector field under a moving reference system and if \mathbf{a}_{opt} is constant within $U_R(\mathbf{x})$. Note that this is the theoretical confirmation of the numerical experiments in [33], which compared the vortex cores in [14] and [33].

4 PATHLINES AND VORTEX CORES

Ideally, vortex cores should be pathlines, i.e., they should be Lagrangian, as discussed in Section 2.4. Existing standard extractors of vortex cores [2, 14, 18, 30, 35, 36, 39] produce vortex cores that are in general not pathlines. In fact, the distance of a vortex core to a pathline is often considered a quality measure for a vortex core [33].

Contrary to existing vortex core extractors, [33] claims that their vortex cores are pathlines, and that deviations are due to numerical errors that can be made vanishing by refining parameters of the numerical method. In particular, [33] claims that $\mathbf{c}_{Ra}(t)$ minimizing Eq. (18) follows a particle trajectory in both \mathbf{v} and the computed optimal Killing

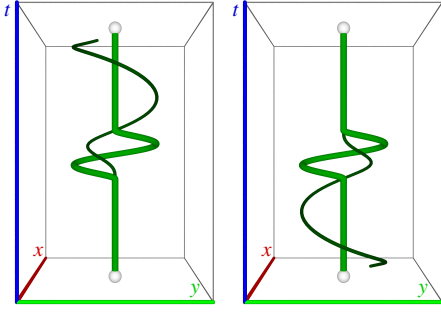


Fig. 2: Space-time visualization of the vortex coreline in Eq. (24) (thick green line), with a pathline (thin green line) seeded from the white sphere in the vector field in Eq. (22) for $k = 0$. On the left, forward integration in \mathbf{v} starting from $(0, 0, -2)$ gives a straight vortex core for $-2 \leq t \leq 0$ but then starts swirling around $(0, 0)$. On the right, backward integration in \mathbf{v} from $(0, 0, 3)$ gives the same in reverse. The deviation of the pathline from the supposed vortex coreline, shows that Eq. (21) does not give a pathline.

field \mathbf{w} . In the following, we show by a counter-example that this claim is incorrect. We define the 2D COUNTER vector field

$$\mathbf{v}(x, y, t) = e^{-k(x^2+y^2)} \begin{pmatrix} -4y \\ 2x - 40s^3 \end{pmatrix} \quad (22)$$

with $(x, y, t) \in [-0.5, 0.5]^2 \times [-2, 3]$, with $k \geq 0$, and

$$s = \begin{cases} t(1-t) & 0 \leq t \leq 1 \\ 0 & \text{else} \end{cases} \quad (23)$$

Note that \mathbf{v} in Eq. (22) is C^∞ continuous in space and C^2 continuous in time. We show that for $k = 0$, \mathbf{v} has a closed-form solution both for $\mathbf{c}_{Ra}(t)$ and the optimal Killing field $\mathbf{a}_{Ra}(t)$:

Lemma 1. *The curve*

$$\mathbf{c}_{Ra}(t) = \begin{pmatrix} x_{Ra}(t) \\ y_{Ra}(t) \end{pmatrix} = \begin{pmatrix} 20s^3 \\ 15s^2(2t-1) \end{pmatrix} \quad (24)$$

along with the optimal Killing field given by

$$\mathbf{a}_{Ra}(t) = \begin{pmatrix} a_{Ra}(t) \\ b_{Ra}(t) \\ \omega_{Ra}(t) \end{pmatrix} = \begin{pmatrix} -60s^2(2t-1) \\ 0 \\ 0 \end{pmatrix} \quad (25)$$

is a local and global minimizer of Eq. (18) for the vector field in Eq. (22) with $k = 0$. In particular it holds $e(\mathbf{c}_{Ra}(t), \mathbf{a}_{Ra}(t), t) = 0$.

Note that this solution neither depends on μ in Eq. (18) nor on the size R of the neighborhood $U_R(\mathbf{x})$ in Eq. (14) as long as they are positive. To prove Lemma 1, we have to show

$$e(\mathbf{x}_{Ra}, \mathbf{a}_{Ra}, t) = 0 \quad (26)$$

$$\nabla_{\mathbf{xa}} e(\mathbf{x}_{Ra}, \mathbf{a}_{Ra}, t) = \mathbf{0} \quad (27)$$

$$\mathbf{H}_{\mathbf{xa}}(\mathbf{x}_{Ra}, \mathbf{a}_{Ra}, t) \text{ is positive definite} \quad (28)$$

where $\nabla_{\mathbf{xa}} e = \left(\frac{\partial e}{\partial x}, \frac{\partial e}{\partial y}, \frac{\partial e}{\partial a}, \frac{\partial e}{\partial b}, \frac{\partial e}{\partial \omega} \right)^T$ is the gradient of e in both the space and the parameters of the Killing field, and $\mathbf{H}_{\mathbf{xa}} = \nabla_{\mathbf{xa}}(\nabla_{\mathbf{xa}} e)$ is the Hessian matrix of e . In the additional material, we show that Eqs. (26)–(28) hold.

Lemma 2. *The curve $\mathbf{c}_{Ra}(t)$ in Eq. (24) is not a pathline of \mathbf{v} with $k = 0$ in Eq. (22).*

To show this, we apply basic differentiation rules to Eqs. (24) and (22), which gives:

$$\dot{\mathbf{c}}_{Ra}(t) = \begin{pmatrix} -60s^2(2t-1) \\ 30s(5s-1) \end{pmatrix} \quad (29)$$

$$\mathbf{v}(\mathbf{c}_{Ra}(t), t) = \mathbf{w}(\mathbf{c}_{Ra}(t), t) = \begin{pmatrix} -60s^2(2t-1) \\ 0 \end{pmatrix} \quad (30)$$

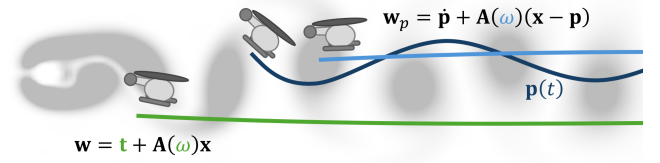


Fig. 3: Conceptual illustration of observer motions (illustrated as helicopters) for our approach (blue) and previous methods [14,20,33] (green). In previous methods, the observer motion \mathbf{w} had three degrees of freedoms: translation $\mathbf{t} = (a(t), b(t))$ and rotation $\omega(t)$. The resulting observer was not necessarily moving along pathlines. With our approach, the translation of the observer motion \mathbf{w}_p is set to follow the pathline $\mathbf{p}(t)$ and only the rotation $\omega(t)$ is unknown. This makes our approach inherently Lagrangian. Here, the light blue trajectory, which is a vortex coreline, will minimize the observed time partial (local minimum of VDE), while the dark blue trajectory will not succeed in making the observed flow steady.

which are not equal, i.e., $\dot{\mathbf{c}}_{Ra}(t) \neq \mathbf{v}(\mathbf{c}_{Ra}(t), t)$. Figure 2 illustrates the vortex coreline that solves Eq. (21) showing that a pathline seeded on the coreline $\mathbf{c}_{Ra}(t)$ leaves after some time.

5 NEW APPROACH - VORTEX DEVIATION ERROR

Lemma 2 showed that none of the existing approaches to extract moving vortex cores is guaranteed to give pathlines. However, being a pathline is one of the common understandings of moving vortex cores. Thus, with this paper we present the – to the best of our knowledge – first approach to extract vortex cores that are guaranteed to be pathlines.

Every moving particle (pathline) can act as vortex core under a suitably chosen moving reference frame. In fact, if the origin of the frame travels with the particle, it remains a static point in the observation. Further, a swirling behavior around it can be observed when choosing the rotation (vorticity) of the Killing field sufficiently large.

Because of this, we present a measure that checks for every pathline $\mathbf{p}(t)$ of the velocity field \mathbf{v} how suitable it is as vortex core. For this, we introduce the *vortex deviation error*

$$\text{VDE}_{\mathbf{p}_0, t_0, \tau} \geq 0 \quad (31)$$

that quantifies how suitable the pathline of \mathbf{v} starting from (\mathbf{p}_0, t_0) integrated over a time interval τ is as a vortex core. The smaller $\text{VDE}_{\mathbf{p}_0, t_0, \tau}$, the better \mathbf{p} acts as vortex core. A perfect vortex core is characterized by $\text{VDE}_{\mathbf{p}_0, t_0, \tau} = 0$.

We share the main idea of [14, 20] to consider the moving reference frames (here represented by Killing fields) and search for minimizers of the observed unsteadiness. However, the difference to existing approaches is as follows: we do not consider all Killing fields but only the subclass that have \mathbf{p} as pathline. With this, we obtain two properties in comparison to existing approaches:

- Vortex cores are guaranteed to be pathlines
- Our Killing field has less degrees of freedom to optimize compared to existing approaches.

The concept and its difference to prior work is illustrated in Figure 3.

5.1 Definition of VDE

Given is a pathline $\mathbf{p} = \mathbf{p}(t)$ of the velocity field $\mathbf{v}(\mathbf{x}, t)$ in the temporal domain $t \in [t_{min}, t_{max}]$, i.e., \mathbf{p} fullfills

$$\dot{\mathbf{p}} = \dot{\mathbf{p}}(t) = \frac{d\mathbf{p}}{dt} = \mathbf{v}(\mathbf{p}(t), t). \quad (32)$$

We define a Killing field \mathbf{w}_p around \mathbf{p} as

$$\mathbf{w}_p = \mathbf{w}_p(\mathbf{x}, \omega, t) = \dot{\mathbf{p}} + \mathbf{A}(\omega)(\mathbf{x} - \mathbf{p}) \quad (33)$$

where $\omega = \omega(t)$ is the unknown vorticity of \mathbf{w}_p .

Lemma 3. *The curve \mathbf{p} is a pathline of both \mathbf{v} and \mathbf{w}_p .*

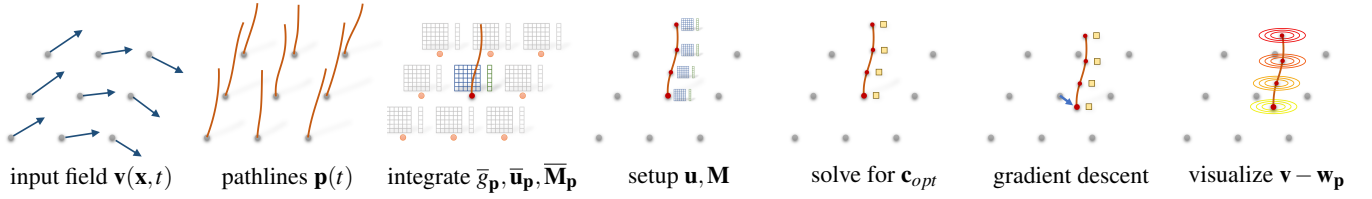


Fig. 4: Overview of the numerical computation pipeline. Given is a time-dependent vector field $\mathbf{v}(\mathbf{x}, t)$. First, calculate pathlines $\mathbf{p}(t)$ for each grid point. At each grid point, spatially integrate $\bar{g}_p, \bar{u}_p, \bar{M}_p$ using Eqs. (53)–(55). If regularization is enabled, also integrate (56)–(58). Next, compute \mathbf{u} and \mathbf{M} of $\hat{e}_{\mathbf{p}_0, t_0, \tau}$, which is detailed in the additional material. Then solve for the optimal observer rotation rates, which are stored along the pathline in \mathbf{c}_{opt} using Eq. (68). Afterwards, discard pathlines along which the observed vorticity is not high enough, see Eq. (71). To reach subvoxel accuracy iterate a gradient descent using Eq. (72). Lastly, visualize the swirling around the vortex coreline in the optimal frame $\mathbf{v} - \mathbf{w}_p$.

The property that \mathbf{p} is a pathline of \mathbf{v} is given by definition in Eq. (32). The proof of \mathbf{p} being a pathline of \mathbf{w}_p can be seen by evaluating \mathbf{w}_p on the pathline, i.e., $\mathbf{w}_p(\mathbf{p}, \omega, t) = \dot{\mathbf{p}}$. Note that the only degree of freedom of \mathbf{w}_p in Eq. (33) is ω . This means that the number of degrees of freedom to be cared for by optimization drops in 2D from 3 for a general Killing field as in Eq. (6) to 1 – the unknown vorticity scalar. In 3D, the number of degrees of freedom for a Killing field drops from 6 to 3 – the unknown vorticity vector.

Similar to [20], we consider the observed time derivative of \mathbf{v} under the reference frame \mathbf{w}_p as

$$\mathbf{m}_p = \mathbf{m}_p(\mathbf{x}, t) = \mathbf{v}_t - \mathbf{w}_{p,t} + \nabla \mathbf{v} \cdot \mathbf{w}_p - \nabla \mathbf{w}_p \cdot \mathbf{v}. \quad (34)$$

Although it was not needed in practice, we provide a regularization that ensures that the optimization obtains a unique solution:

$$\mathbf{m}_{r,p} = \mathbf{m}_{r,p}(\mathbf{x}, \omega, t) = \mathbf{v} - \mathbf{w}_p. \quad (35)$$

Note that a similar measure as in (35) is used in [20] for regularization and in [26] as a full measure of interest. We compute the accumulated observed unsteadiness error in a R -neighborhood around \mathbf{p} :

$$e_p(\omega, t) = \frac{1}{A} \int_{U_R(\mathbf{p}(t))} \mathbf{m}_p^T \mathbf{m}_p \, dx \quad (36)$$

$$e_{r,p}(\omega, t) = \frac{1}{A} \int_{U_R(\mathbf{p}(t))} \mathbf{m}_{r,p}^T \mathbf{m}_{r,p} \, dx \quad (37)$$

with $A = \text{area}(U_R(\mathbf{p}(t)))$ being the area/volume of the R -neighborhood U_R around \mathbf{p} . Note that $e_p, e_{r,p}$ describe the accumulated error in the neighborhood of $\mathbf{p}(t)$ for every t . For the entire pathline, we consider its integral over the temporal domain

$$\hat{e}_{\mathbf{p}_0, t_0, \tau}(\omega) = \frac{1}{\tau} \int_{t_0}^{t_0 + \tau} e_p + \varepsilon e_{r,p} \, dt \quad (38)$$

with $\mathbf{p}_0 = \mathbf{p}(t_0)$ and ε is a small number determining the influence of the regularization. In all examples in the paper, we left $\varepsilon = 0$. We search for the function $\omega(t)$ that minimizes $\hat{e}_{\mathbf{p}_0, t_0, \tau}$:

$$\omega_{opt} = \omega_{opt}(t) = \underset{\omega(t) \in C^1([t_0, t_0 + \tau])}{\operatorname{argmin}} \hat{e}_{\mathbf{p}_0, t_0, \tau}(\omega). \quad (39)$$

Note that Eq. (39) is a variational optimization in the unknown function $\omega(t)$, as it contains both $\omega(t)$ and $\dot{\omega}(t)$. Thus, we solve the Euler-Lagrange equations [12], which are a necessary condition for the optimum of Eq. (39):

$$\frac{\delta \hat{e}_{\mathbf{p}_0, t_0, \tau}(\omega)}{\delta \omega(t)} = \frac{\partial \hat{e}_{\mathbf{p}_0, t_0, \tau}(\omega)}{\partial \omega} - \frac{d}{dt} \left(\frac{\partial \hat{e}_{\mathbf{p}_0, t_0, \tau}(\omega)}{\partial \dot{\omega}} \right) = 0 \quad (40)$$

As we will show later, the equation can be solved linearly upon discretization. With this we define the final vortex deviation error as

$$\text{VDE}_{\mathbf{p}_0, t_0, \tau} = \hat{e}_{\mathbf{p}_0, t_0, \tau}(\omega_{opt}). \quad (41)$$

5.2 Properties of VDE

Theorem 1. $\text{VDE}_{\mathbf{p}_0, t_0, \tau}$ is objective.

This follows directly from the objectivity of $\mathbf{m}_p, \mathbf{m}_{r,p}$ in Eqs. (34)–(35) that was shown in [20].

Theorem 2. $\text{VDE}_{\mathbf{p}_0, t_0, \tau}$ is Lagrangian.

This follows from Eq. (38), showing that the subject of optimization is an integration over a whole pathline.

5.3 Numerical computation of VDE

VDE produces a scalar field. The core of the VDE computation is the solution of the variational optimization in Eq. (39). To calculate vortex corelines from VDE, we take the following steps:

1. computation of e_p and $e_{r,p}$ on a discrete grid, cf. Eqs. (36)–(37).
2. discretization of $\hat{e}_{\mathbf{p}_0, t_0, \tau}$ along pathlines seeded at grid vertices
3. solution of (39) as minimizer of a quadratic equation per pathline
4. apply filter criteria to pathlines and determine local minima
5. gradient descent of pathline seed to achieve subvoxel accuracy

In the following, we describe the steps in detail.

5.3.1 Computation of e_p and $e_{r,p}$

Eqs. (33)–(34) give that \mathbf{m}_p depends linearly on the unknowns $\omega, \dot{\omega}$. This means that by writing the unknowns in a vector \mathbf{a} by

$$\mathbf{a} = \mathbf{a}(t) = (\omega(t), \dot{\omega}(t))^T, \quad (42)$$

we can rewrite \mathbf{m}_p in Eq. (34) and $\mathbf{m}_{r,p}$ in Eq. (35) in the form

$$\mathbf{m}_p = \dot{\mathbf{v}}_p - \mathbf{M}_p \mathbf{a}, \quad \mathbf{m}_{r,p} = \dot{\mathbf{v}}_{r,p} - \mathbf{M}_{r,p} \mathbf{a} \quad (43)$$

Thereby, $\dot{\mathbf{v}}_p$ and $\dot{\mathbf{v}}_{r,p}$ have a simple form:

$$\dot{\mathbf{v}}_p = \dot{\mathbf{v}}_p(\mathbf{x}, t) = \mathbf{J} \dot{\mathbf{p}} + \mathbf{v}_t - \ddot{\mathbf{p}}, \quad \dot{\mathbf{v}}_{r,p} = \dot{\mathbf{v}}_{r,p}(\mathbf{x}, t) = \mathbf{v} - \dot{\mathbf{p}}. \quad (44)$$

In 2D, the matrices \mathbf{M}_p and $\mathbf{M}_{r,p}$ are:

$$\mathbf{M}_p = \mathbf{M}_p(\mathbf{x}, t) = (\mathbf{J} \mathbf{Q} \Delta \mathbf{x} - \mathbf{Q} \Delta \mathbf{v}, -\mathbf{Q} \Delta \mathbf{x}) \quad (45)$$

$$\mathbf{M}_{r,p} = \mathbf{M}_{r,p}(\mathbf{x}, t) = (-\mathbf{Q} \cdot (\mathbf{x} - \mathbf{p}), \mathbf{0}_2) \quad (46)$$

whereas in 3D, the matrices \mathbf{M}_p and $\mathbf{M}_{r,p}$ are:

$$\mathbf{M}_p = \mathbf{M}_p(\mathbf{x}, t) = (\mathbf{J} \mathbf{A}(\Delta \mathbf{x}) - \mathbf{A}(\Delta \mathbf{v}), -\mathbf{A}(\Delta \mathbf{x})) \quad (47)$$

$$\mathbf{M}_{r,p} = \mathbf{M}_{r,p}(\mathbf{x}, t) = (-\mathbf{A}(\mathbf{x} - \mathbf{p}), \mathbf{0}_{3 \times 3}) \quad (48)$$

with the following short-hand notations:

$$\ddot{\mathbf{p}} = \ddot{\mathbf{p}}(t) = \nabla \mathbf{v}(\mathbf{p}, t) \mathbf{v}(\mathbf{p}, t) + \mathbf{v}_t(\mathbf{p}, t) \quad (49)$$

$$\Delta \mathbf{x} = \Delta \mathbf{x}(\mathbf{x}, t) = \mathbf{x} - \mathbf{p} \quad (50)$$

$$\Delta \mathbf{v} = \Delta \mathbf{v}(\mathbf{x}, t) = \mathbf{v} - \dot{\mathbf{p}} = \mathbf{v}(\mathbf{x}, t) - \mathbf{v}(\mathbf{p}, t) \quad (51)$$

The proof that \mathbf{m}_p in Eq. (34) and $\mathbf{m}_{r,p}$ in Eq. (35) are identical to Eqs. (43)–(51) is provided in the additional material.

Inserting Eq. (43) into Eq. (36) gives that e_p and $e_{r,p}$ depend quadratically on the unknown $\omega, \dot{\omega}$ and can therefore be written in the form

$$e_p = \bar{g}_p - 2\bar{\mathbf{u}}_p^T \mathbf{a} + \mathbf{a}^T \bar{\mathbf{M}}_p \mathbf{a}, \quad e_{r,p} = \bar{g}_{r,p} - 2\bar{\mathbf{u}}_{r,p}^T \mathbf{a} + \mathbf{a}^T \bar{\mathbf{M}}_{r,p} \mathbf{a} \quad (52)$$

with the coefficients of the quadratic form being

$$\bar{g}_p = \bar{g}_p(t) = \frac{1}{A} \int_{U_R(\mathbf{p}(t))} \dot{\mathbf{v}}_p(\mathbf{x}, t)^T \dot{\mathbf{v}}_p(\mathbf{x}, t) d\mathbf{x} \quad (53)$$

$$\bar{\mathbf{u}}_p = \bar{\mathbf{u}}_p(t) = \frac{1}{A} \int_{U_R(\mathbf{p}(t))} \mathbf{M}_p(\mathbf{x}, t)^T \dot{\mathbf{v}}_p(\mathbf{x}, t) d\mathbf{x} \quad (54)$$

$$\bar{\mathbf{M}}_p = \bar{\mathbf{M}}_p(t) = \frac{1}{A} \int_{U_R(\mathbf{p}(t))} \mathbf{M}_p(\mathbf{x}, t)^T \mathbf{M}_p(\mathbf{x}, t) d\mathbf{x} \quad (55)$$

and with the coefficients of the (optional) regularization term being

$$\bar{g}_{r,p} = \bar{g}_{r,p}(t) = \frac{1}{A} \int_{U_R(\mathbf{p}(t))} \dot{\mathbf{v}}_{r,p}(\mathbf{x}, t)^T \dot{\mathbf{v}}_{r,p}(\mathbf{x}, t) d\mathbf{x} \quad (56)$$

$$\bar{\mathbf{u}}_{r,p} = \bar{\mathbf{u}}_{r,p}(t) = \frac{1}{A} \int_{U_R(\mathbf{p}(t))} \mathbf{M}_{r,p}(\mathbf{x}, t)^T \dot{\mathbf{v}}_{r,p}(\mathbf{x}, t) d\mathbf{x} \quad (57)$$

$$\bar{\mathbf{M}}_{r,p} = \bar{\mathbf{M}}_{r,p}(t) = \frac{1}{A} \int_{U_R(\mathbf{p}(t))} \mathbf{M}_{r,p}(\mathbf{x}, t)^T \mathbf{M}_{r,p}(\mathbf{x}, t) d\mathbf{x}. \quad (58)$$

5.3.2 Discretization of $\hat{e}_{\mathbf{p}_0, t_0, \tau}$

To integrate the measure over time along the pathline, we sample $\mathbf{p}(t)$ regularly in time at the $N+1$ sample times

$$t_i = \left(1 - \frac{i}{N}\right) t_0 + \frac{i}{N} (t_0 + \tau) \quad (59)$$

for $i = 0, \dots, N$, resulting in

$$\mathbf{p}_i = \mathbf{p}(t_i), \quad \bar{g}_i = \bar{g}_p(t_i) + \varepsilon \bar{g}_{r,p}(t_i) \quad (60)$$

$$\bar{\mathbf{u}}_i = \bar{\mathbf{u}}_p(t_i) + \varepsilon \bar{\mathbf{u}}_{r,p}(t_i), \quad \bar{\mathbf{M}}_i = \bar{\mathbf{M}}_p(t_i) + \varepsilon \bar{\mathbf{M}}_{r,p}(t_i). \quad (61)$$

By further setting $\mathbf{a}_i = (\omega_i, \dot{\omega}_i)^T$, we get as discretization of Eq. (38)

$$\hat{e}_{\mathbf{p}_0, t_0, \tau} = \frac{1}{N+1} \sum_{i=0}^N \left(\bar{g}_i - 2\bar{\mathbf{u}}_i^T \mathbf{a}_i + \mathbf{a}_i^T \bar{\mathbf{M}}_i \mathbf{a}_i \right). \quad (62)$$

Note that $\hat{e}_{\mathbf{p}_0, t_0, \tau}$ in Eq. (62) depends quadratically on the unknowns $\omega_0, \dots, \omega_N, \dot{\omega}_0, \dots, \dot{\omega}_N$. In 2D, we introduce the vector of unknowns

$$\mathbf{c} = (\omega_0, \dots, \omega_N)^T, \quad (63)$$

and we assume that the sampling is dense enough such that the derivatives can be computed by a linear operator

$$\dot{\mathbf{c}} = (\dot{\omega}_0, \dots, \dot{\omega}_N)^T = \mathbf{L} \mathbf{c} \quad (64)$$

where \mathbf{L} is an $(N+1) \times (N+1)$ matrix, which is listed in the additional material. In 3D, the vector of unknowns stacks the three components of the unknown vorticity vector:

$$\mathbf{c} = (\omega_0[1], \dots, \omega_N[1], \omega_0[2], \dots, \omega_N[2], \omega_0[3], \dots, \omega_N[3])^T, \quad (65)$$

and the derivatives are similarly given by a linear operator

$$\begin{aligned} \dot{\mathbf{c}} &= (\dot{\omega}_0[1], \dots, \dot{\omega}_N[1], \dot{\omega}_0[2], \dots, \dot{\omega}_N[2], \dot{\omega}_0[3], \dots, \dot{\omega}_N[3])^T \\ &= \begin{pmatrix} \mathbf{L} & \mathbf{0} & \mathbf{0} \\ \mathbf{0} & \mathbf{L} & \mathbf{0} \\ \mathbf{0} & \mathbf{0} & \mathbf{L} \end{pmatrix} \mathbf{c}. \end{aligned} \quad (66)$$

This allows to rewrite Eq. (62) compactly in matrix form

$$\hat{e}_{\mathbf{p}_0, t_0, \tau} = g - 2\mathbf{u}^T \mathbf{c} + \mathbf{c}^T \mathbf{M} \mathbf{c} \quad (67)$$

where \mathbf{c} contains the unknowns, and where $g, \mathbf{u}, \mathbf{M}$ are computed from information along and around the pathline. The additional material provides the details on how to set up g, \mathbf{u} , and \mathbf{M} .

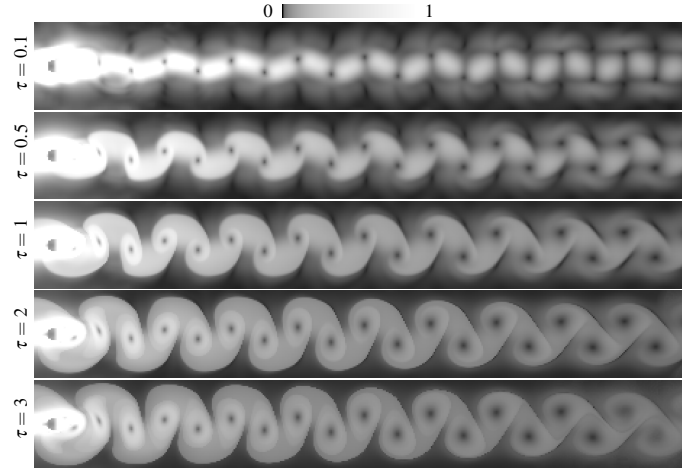


Fig. 5: Visualization of the VDE field for varying integration durations τ . With sufficiently long integration duration, VDE minima appear.

5.3.3 Solution of Eq. (39)

To finally solve the variational optimization in Eq. (39), we have to solve Eq. (67) for the unknown \mathbf{c} . This gives

$$\mathbf{c}_{opt} = \mathbf{M}^{-1} \mathbf{u}. \quad (68)$$

Rather than computing the inverse of \mathbf{M} , we perform a sparse Cholesky decomposition and backsubstitute. From this, we obtain VDE as:

$$\text{VDE}_{\mathbf{p}_0, t_0, \tau} = g - 2\mathbf{u}^T \mathbf{c}_{opt} + \mathbf{c}_{opt}^T \mathbf{M} \mathbf{c}_{opt} \quad (69)$$

$$= g - \mathbf{u}^T \mathbf{M}^{-1} \mathbf{u}. \quad (70)$$

Note that in \mathbf{M} the consideration of the regularization (i.e., $\varepsilon > 0$) guarantees that \mathbf{M} has full rank. This is because $e_{r,p}$ in Eq. (37) depends only on ω and not on $\dot{\omega}$. This means that the optimal ω for $e_{r,p}$ can be computed for each time step independently, resulting in a full-rank system matrix as shown in [20]. In practice, it turned out that this regularization was never needed, since the linear systems always had full rank, and hence we kept $\varepsilon = 0$ in all examples in the paper.

5.3.4 Filtering

VDE produces a scalar field, in which local minima are of interest. Fig. 5 displays the scalar field in the CYLINDER flow for different integration durations τ , showing how the minima become more distinguishable. To restrict the VDE minima extraction to vortex corelines in an objective manner, we require the instantaneous vorticity deviation [22] to be sufficiently high for all vertices along the pathline:

$$\omega_{\min} \leq \left\| \omega_{\mathbf{v}(t_i)} - \frac{1}{|U|} \int_U \omega(\mathbf{y}, t_i) d\mathbf{y} \right\|, \quad \forall i \in \{0, \dots, N\} \quad (71)$$

where U is the spatial domain of the data set. The threshold ω_{\min} thereby acts as swirling strength criterion. Increasing the threshold limits the extraction to vortices that exhibit a sufficiently strong rotation rate. Figure 6 shows the impact of the filter.

5.3.5 Gradient descent

Calculating VDE on a discrete grid limits the accuracy of the extracted vortex corelines to the spacing between grid points. To reach subvoxel accuracy, we take the local minima on the grid as seed points and perform a gradient descent optimization of the seed point \mathbf{p}_0 :

$$\mathbf{p}_0^{i+1} \approx \mathbf{p}_0^i - h \cdot \frac{\partial \hat{e}_{\mathbf{p}_0, t_0, \tau}(\omega_{opt})}{\partial \mathbf{p}_0} \quad (72)$$

The required partial derivatives are estimated with second-order central differences. In all data sets, we performed 10 iterations of gradient descent, which proved sufficient to converge, since the initial guess is close to the optimum, namely within the grid spacing, see Fig. 7.

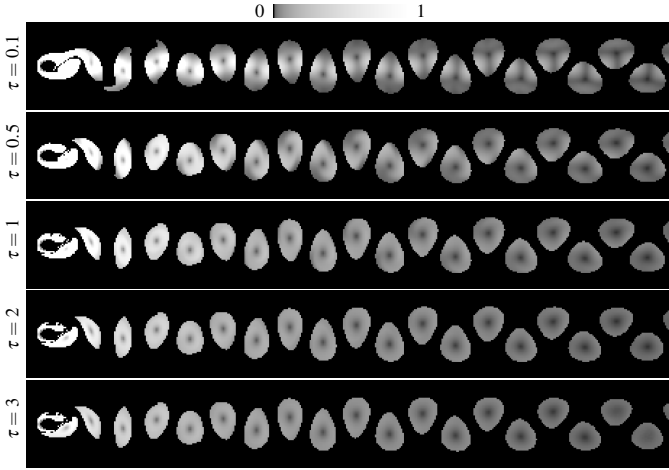


Fig. 6: Visualization of the impact of filtering at different integration durations τ . Regions are masked out if the instantaneous vorticity deviation is below $\omega_{\min} = 2$ at any point along the pathline. Valid regions are visible early, but they become more stable with longer integration durations.

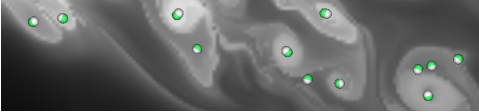


Fig. 7: Impact of gradient descent: before (green), after (white).

6 VISUAL REPRESENTATION

The development of a visual representation for moving vortex cores is challenging because it requests the simultaneous encoding of the following features and properties.

- Movement of vortex cores: vortex cores move over time on trajectories (pathlines). In addition, moving vortex cores in 3D may change their shapes.
- Swirling around vortex cores: finding a visual representation of the swirling behavior around the vortex cores is crucial for understanding the vortical behavior.

Existing approaches to extract vortex cores [2, 14, 18, 30, 35, 36, 39] focus on the visual representation of the core movement. Recently, Rautek et al. [33] presented an approach to represent both aspects in the following way: the movement of a 2D vortex core is represented by a 3D space-time curve, and the swirling behavior is shown by a 2D LIC of $\mathbf{v} - \mathbf{w}_{opt}$. Unfortunately, the approach in [33] does not carry over to 3D flows because of the following reasons: First, moving 3D vortex cores are surfaces in 4D space-time, for which no straightforward visual representation exists. Second, while 3D LIC approaches exist, their applicability in comparison to 2D LIC is strongly limited due to reasons of perception.

Our visual representation is a combination of several characteristic curves: streamlines, pathlines, and extremal lines. With this, our approach is applicable in both 2D and 3D.

2D View We represent a local minimum of $VDE_{\mathbf{x},t_0,\tau}$ in \mathbf{x} as a white point \mathbf{p}_0 . Further, we represent the pathline $\mathbf{p}(t)$ starting at (\mathbf{p}_0, t_0) over the time interval $[t_0, t_0 + \tau]$ as a blue curve – the moving vortex core. We sample the time interval $[t_0, t_0 + \tau]$ regularly at n_t sample points t_i with $i = 1, \dots, n_t$, and compute streamlines of the field

$$\mathbf{v}(\mathbf{x}, t_i) - \mathbf{w}_p(\mathbf{x}, \omega_{opt}, t_i) \quad (73)$$

seeded around the point $(\mathbf{p}(t_i), t_i)$ using [25]. These streamlines are color coded according to time t_i on a yellow-orange-red color scale, and they encode the swirling direction around the vortex core at the times t_i by an increasing line width. For context, we visualize the (filtered) field $VDE_{\mathbf{x},t_0,\tau}$ in the background using a gray scale.

3D View We extract an extremal curve of $VDE_{\mathbf{x},t_0,\tau}$ using [8], depict it as blue curve (the vortex core at t_0), and sample it at n_x points $\mathbf{p}_{0,j}$ for $j = 1, \dots, n_x$. Similar to the 2D case, we consider the pathlines $\mathbf{p}_j(t)$ starting at $(\mathbf{p}_{0,j}, t_0)$, and visualize streamlines of the vector field

$$\mathbf{v}(\mathbf{x}, t_i) - \mathbf{w}_p(\mathbf{x}, \omega_{opt}, t_i) \quad (74)$$

seeded around the point $(\mathbf{p}_j(t_i), t_i)$, for $i = 1, \dots, n_t, j = 1, \dots, n_x$. Similar to the 2D case, these streamlines represent the swirling behavior around the vortex cores at time t_i , and are color coded according to t_i . For context, we additionally show a volume rendering of the (filtered) field $VDE_{\mathbf{x},t_0,\tau}$ in the background. In this paper, we set $n_t = 4, n_x = 10$.

7 RESULTS

In the following section, we demonstrate our method on several 2D and 3D vector fields, we study the impact of the parameters, we provide detailed performance measurements for all examples shown in the paper, and we discuss the properties and limitations of our method. We published a reference implementation [19] of VDE for the CYLINDER flow with which Fig. 5 can be reproduced.

7.1 Counter Example 2D

In Section 4, we constructed a counter example to show that vortex corelines of Rautek et al. [33] are not necessarily pathlines. In Fig. 8, we show results of our method on the COUNTER data set, using our proposed 2D view (left) and a space-time visualization (right). The light blue line shows the vortex coreline of our method for $t_0 = -1.5$, $\tau = 4$, and $k = 1$. The dark blue pathline is indeed swirling around the vortex coreline, but due to the slow rotational speed, this is difficult to recognize, especially since the vortex is moving itself. In contrast, the swirling streamlines display the rotating motion in the observed vector field at selected time steps well. In contrast to Rautek et al. [33], our vortex coreline is indeed a pathline of the flow, along which swirling motion is encountered.

7.2 Cylinder 2D

The CYLINDER data set is a frequently used vortex extraction benchmark, since the path of vortices is well-understood. The flow was simulated with Gerris flow solver [31] and contains a von-Kármán vortex street with Reynolds number 160. Vortices are periodically shedding from the circular obstacle. The data set was made available by Günther et al. [14]. The results of our method are shown in Fig. 9 for different neighborhood regions R , which are measured in voxels. The background shows the filtered VDE slice, on which the local minima are displayed from which pathline integration is started, resulting in the light blue vortex corelines. The streamlines in the observed steady vector field, display for four different time steps the swirling motion

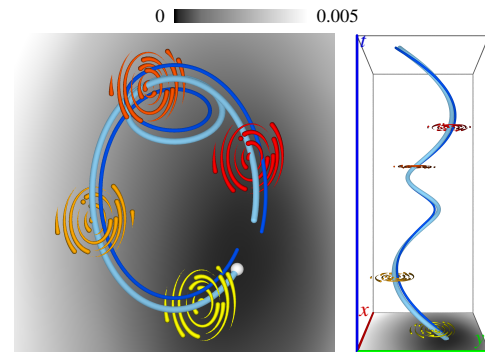


Fig. 8: Visualization of the vortex coreline using our method in the COUNTER flow. On the left, a 2D view is shown which displays swirling streamlines at selected time slices along the vortex coreline (light blue). The streamline color encodes time. To demonstrate the swirling, a nearby pathline (dark blue) is seeded nearby, which remains close and exhibits swirling motion. On the right, a space-time visualization of this data set is shown, in which time is mapped to the vertical axis.

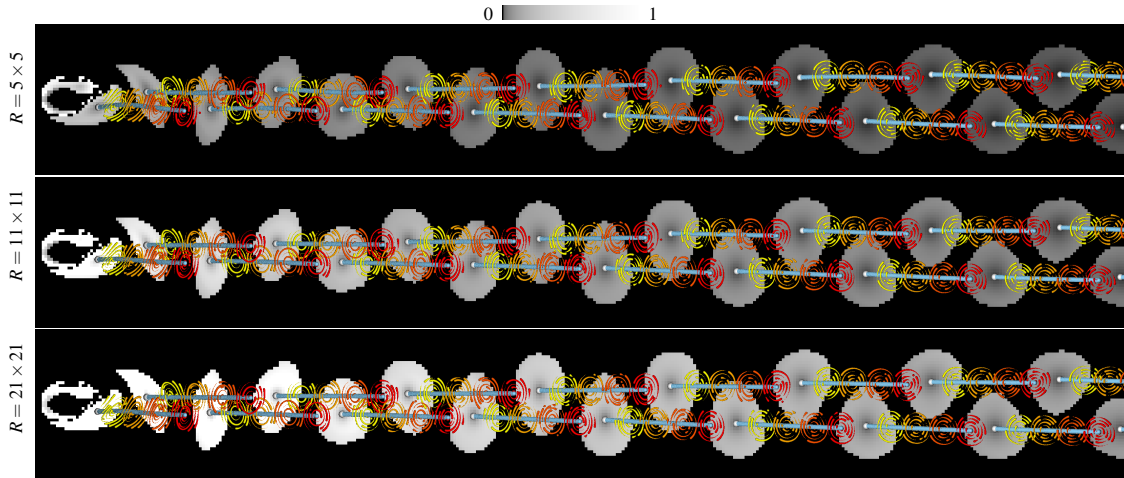


Fig. 9: Vortex coreline visualization using VDE in the CYLINDER2D flow. Here, vortices are known to move with almost equal speed from left to right, i.e., they perform near-Galilean transformations. To visualize the swirling motion, we display streamlines in the observed vector field $\mathbf{v}(\mathbf{x}) - \mathbf{w}_p(\mathbf{x})$ along the vortex corelines at time steps chosen such that visual clutter is avoided. Streamlines with the same color exist at the same time. The VDE slice is calculated for $t_0 = 12$ and $\tau = 2$ for varying neighborhood sizes. The required minimal IVD ω_{\min} was set to 2 to limit the search for VDE minima to regions within the vortices. Vortex corelines are detected for all neighborhood sizes. The larger R the higher is the absolute time partial residual.

around the vortex corelines. For small choices of R , the value range is generally lower than for the fitting of an observer to a larger region. If R is high enough, the VDE minima are well visible. In Fig. 5, we displayed VDE for different integration durations and in Fig. 6, we demonstrated the output after application of the instantaneous vorticity deviation filter. See the supplemental video for varying start times t_0 .

7.3 Boussinesq 2D

A more complex example is the BOUSSINESQ flow, which was likewise simulated with Gerris flow solver [31]. It contains a flow rising from a heated cylinder. The data set was provided by [14]. In this flow, small vortices are generated, which even spiral around each other. To capture those intricate details, small neighborhood windows are required. In Fig. 10, we provide a parameter study of the instantaneous vorticity deviation threshold ω_{\min} , which we apply to limit the search for local VDE minima. In the figure, the threshold is increased from left to right. Two things are noticeable: (1) As the threshold increases, weak vortices are gradually removed. (2) The result is rather threshold-insensitive for higher values of ω_{\min} .

7.4 Square Cylinder 3D

The SQUARE CYLINDER flow of Weinkauff et al. [6,39] contains a three-dimensional von-Kármán vortex street. The vortex axes are almost orthogonal to the flow direction, which makes this a case in which multiple time steps can be illustrated well without occlusion. Fig. 1 shows results of our approach. The vortex cores sweep over time along a path surface. At selected timelines, the streamlines of the optimal frame are visualized, which conveys the rotating motion.

7.5 Vortex Rings 3D

Lastly, Fig. 11 shows two VORTEX RINGS that rise in a buoyant fluid flow. The upper vortex retains its ring shape over time, while the lower vortex core breaks down into a horseshoe vortex. Since the path of our vortex cores are the result of a path surface integration, vortex cores are easy to track over time, despite the vortex breakdown. The display of swirling streamlines in future time steps conveys the path of the vortex corelines and indicates the swirling motion that is present around them.

7.6 Performance

In the following, we list in Table 1 the parameters and the performance measurements for all data sets shown in the paper. The measurements have been taken on a workstation with an Intel Core i9-10980XE CPU with 3.00 GHz. Where the bottleneck occurs depends on the parameters and the resolution. The experiments on the CYLINDER have shown that

the spatial integration of $\bar{\mathbf{g}}_p$, $\bar{\mathbf{u}}_p$, and $\bar{\mathbf{M}}_p$ in Eqs. (53)–(55) becomes costly for large neighborhood regions R . We have parallelized over the grid points, but for each grid point we loop sequentially over its neighborhood region. An acceleration with summed area tables similar to [14] is not straightforward, since each grid point has its own pathline around which the spatial integrals are formed. The experiments on the CYLINDER flow have also shown that the cost for setting up and solving the linear system is increasing with the number of pathline sample points, as well. In general, the complexity of linear solvers increases cubically in the number of unknowns. The extraction of extremal structures and the gradient descent refinement are negligible in comparison. In the 2D flows, we obtained results at the order of a few seconds. Since the 3D flows have more voxels, the computation time increased to the order of minutes.

7.7 Discussion

Locality of Optimal Observers Our method calculates unsteadiness minimizing reference frames successfully only along critical paths in the observed flow, e.g., along vortex corelines. In all other regions of the domain, the optimal near-steady observer does not necessarily follow along pathlines. Thus, if the near-steady flow should be observed elsewhere in the domain, then previous reference frame optimization methods [14, 20, 33] would be a suitable choice.

Parameters Our method depends on three key parameters: the start time t_0 , the integration duration τ , and the size of the neighborhood region R . All three have been studied either in the paper (τ and R) or in the supplemental video (t_0). Further, the numerical parameters (integration step size, sampling rate along pathline) have to be chosen with care to avoid numerical errors. This, however, is standard practice in flow visualization and is likewise done for any other metric based on particle paths, such as FTLE.

Temporal Aggregation VDE is inherently a Lagrangian metric. Lagrangian metrics have the disadvantage that they aggregate information about a particle’s experience over time into a single number. This entails that VDE might exhibit a high value even though the vorticity is not high at all time steps. In fact, VDE cannot tell when vortices dissipate. VDE has this limitation in common with other Lagrangian metrics. For example, FTLE does likewise not express when (and where) a separation has occurred in a given time interval.

Temporal Stability A major benefit of Lagrangian methods is their very high temporal stability, which is visible in the supplemental video. Our vortex corelines are guaranteed to move along particle paths. Thus, vortex cores are sweeping smoothly through the domain.

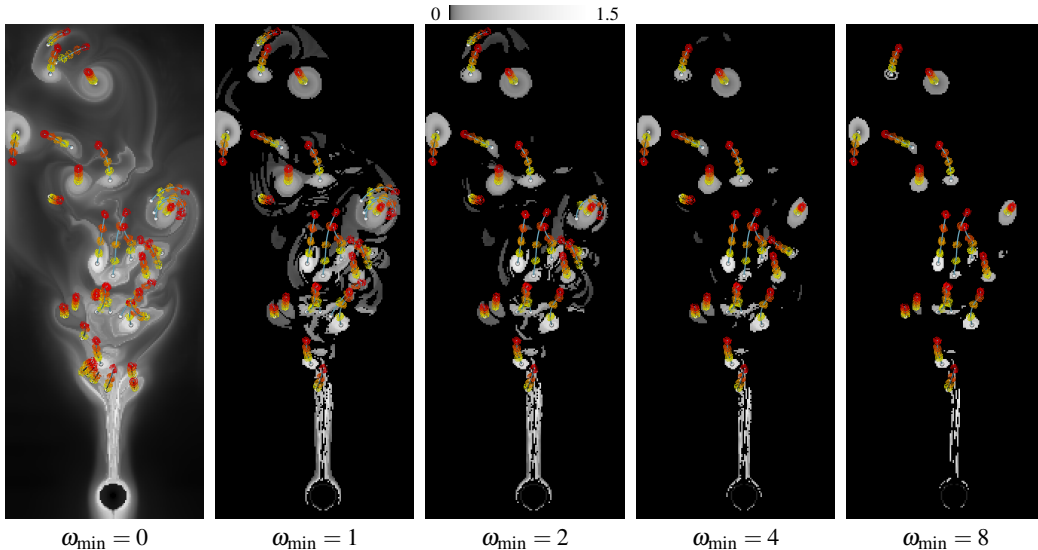


Fig. 10: Parameter study of the instantaneous vorticity deviation threshold ω_{\min} in the BOUSSINESQ flow. The threshold is applied to remove vortices that exhibit too low swirling strength throughout the time interval. In the image center, nearby vortices can be seen to rotate around each other. Throughout the domain, vortices exhibit different movement directions, which is why a different observer needs to be searched per vortex coreline.

Data set	Figure	Resolution	R	t_0	τ	$N+1$	ω_{\min}	$\bar{g}_p, \bar{u}_p, \bar{M}_p$	$\mathbf{u}, \mathbf{M}, \mathbf{c}_{opt}$	coreline
CYLINDER	Fig. 5/6(a)	640×80	11×11	12	0.1	10	0/2	0.12	0.20	–
CYLINDER	Fig. 5/6(b)	640×80	11×11	12	0.5	50	0/2	0.58	0.57	–
CYLINDER	Fig. 5/6(c)	640×80	11×11	12	1	100	0/2	1.16	0.76	–
CYLINDER	Fig. 5/6(d)	640×80	11×11	12	2	200	0/2	2.33	1.27	–
CYLINDER	Fig. 5/6(e)	640×80	11×11	12	3	300	0/2	3.49	2.02	–
COUNTER	Fig. 8	50×50	11×11	-1.5	4	400	0	0.02	0.40	0.28
CYLINDER	Fig. 9(a)	640×80	5×5	12	2	200	2	0.56	1.33	1.41
CYLINDER	Fig. 9(b)	640×80	11×11	12	2	200	2	2.32	1.32	1.43
CYLINDER	Fig. 9(c)	640×80	21×21	12	2	200	2	8.04	1.31	1.55
BOUSSINESQ	Fig. 10(a)-(e)	150×450	11×11	10	2	200	0/1/2/4/8	3.22	1.96	4.99
SQUARE CYL.	Fig. 1	$192 \times 64 \times 48$	$11 \times 11 \times 11$	64	5	50	0.2	67.18	222.75	12.3
VORTEX RINGS	Fig. 11	$94 \times 190 \times 94$	$11 \times 11 \times 11$	3.78	0.67	20	2	265.42	43.02	9.39

Table 1: Performance measurements for all data sets in seconds. The parameters are the size of the neighborhood R , start time t_0 , integration duration τ , number of vertices along pathline $N+1$, and the instantaneous vorticity deviation threshold ω_{\min} . The timings are listed for the spatial integration of $\bar{g}_p, \bar{u}_p, \bar{M}_p$ (which are needed for e_p), the integration of \mathbf{u}, \mathbf{M} along the pathline and solving for \mathbf{c}_{opt} which optimizes $\hat{e}_{p0,t_0,\tau}$, and lastly for the search for the local minima/valley lines of VDE including the gradient descent to reach subvoxel accuracy.

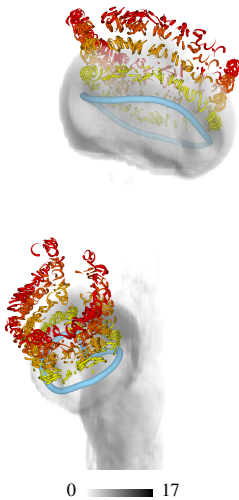


Fig. 11: Visualization of two VORTEX RINGS. The upper vortex retains its ring shape, while the lower vortex breaks into a horseshoe vortex.

8 CONCLUSIONS

In this paper, we discussed the theoretical similarities of recent objectivization methods [14, 33] and we have shown that neither of them is guaranteed to extract vortex corelines that are Lagrangian. Afterwards, we proposed the first Lagrangian vortex coreline extraction algorithm, which optimizes for the optimal observer rotation for observers that are restricted to move along pathlines. The optimal rotation rate is solved variationally as function along the entire pathline, for which we derived a linear system. To depict the swirling motion around the vortex cores in 2D and 3D flow, we proposed to visualize the swirling motion using streamlines in the observed vector field at selected time steps. We demonstrated the approach in several 2D and 3D vector fields.

At present, the algorithm is implemented on the CPU with OpenMP parallelization. In the future, it would be imaginable to parallelize the computation on the GPU. Further, the placement of streamlines could be optimized to convey the rotating motion while reducing occlusions. We plan to investigate how the integration duration is tied to the time scale and how the neighborhood size is tied to length scales of vortices.

Acknowledgments

This work was partially supported by DFG grant no. GU 945/3-1.

REFERENCES

- [1] G. Astarita. Objective and generally applicable criteria for flow classification. *Journal of Non-Newtonian Fluid Mechanics*, 6(1):69–76, 1979. doi: [10.1016/0377-0257\(79\)87004-4](https://doi.org/10.1016/0377-0257(79)87004-4) 2
- [2] I. Baeza Rojo and T. Günther. Vector field topology of time-dependent flows in a steady reference frame. *IEEE Transactions on Visualization and Computer Graphics*, 26(1):280–290, 2020. doi: [10.1109/TVCG.2019.2934375](https://doi.org/10.1109/TVCG.2019.2934375) 2, 3, 7
- [3] D. C. Banks and B. A. Singer. A predictor-corrector technique for visualizing unsteady flow. *IEEE Transactions on Visualization and Computer Graphics*, 1:151–163, 1995. doi: [10.1109/2945.468404](https://doi.org/10.1109/2945.468404) 2
- [4] R. Bujack, L. Yan, I. Hotz, C. Garth, and B. Wang. State of the art in time-dependent flow topology: Interpreting physical meaningfulness through mathematical properties. *Computer Graphics Forum*, 39(3):811–835, 2020. doi: [10.1111/cgf.14037](https://doi.org/10.1111/cgf.14037) 1
- [5] B. Cabral and L. C. Leedom. Imaging vector fields using line integral convolution. In *Proceedings of the 20th Annual Conference on Computer Graphics and Interactive Techniques, SIGGRAPH '93*, 8 pages, p. 263–270. Association for Computing Machinery, New York, NY, USA, 1993. doi: [10.1145/166117.166151](https://doi.org/10.1145/166117.166151) 1
- [6] S. Camarri, A. Iollo, M. Buffoni, and M. V. Salvetti. Simulation of the three-dimensional flow around a square cylinder between parallel walls at moderate Reynolds numbers. In *XVII Congresso di Meccanica Teorica ed Applicata*, pp. 1–12. Firenze University Press, Florence, Italy, 2005. doi: [10.1400/56904](https://doi.org/10.1400/56904) 8
- [7] M. S. Chong, A. E. Perry, and B. J. Cantwell. A general classification of three-dimensional flow fields. *Physics of Fluids A: Fluid Dynamics*, 2(5):765–777, 1990. doi: [10.1063/1.857730](https://doi.org/10.1063/1.857730) 2
- [8] N. DaBler and T. Günther. Variational feature extraction in scientific visualization. *ACM Transactions on Graphics (SIGGRAPH)*, 43(4):109:1–109:16, 2024. doi: [10.1145/3658219](https://doi.org/10.1145/3658219) 7
- [9] R. Drouot and M. Lucius. Approximation du second ordre de la loi de comportement des fluides simples. Lois classiques déduites de l'introduction d'un nouveau tenseur objectif. *Archivum Mechaniki Stosowanej*, 28(2):189–198, 1976. 2
- [10] A. Friederici, H. Theisel, and T. Günther. Trajectory vorticity - computation and visualization of rotational trajectory behavior in an objective way. *IEEE Transactions on Visualization and Computer Graphics*, 2024. doi: [10.1109/TVCG.2024.3421555](https://doi.org/10.1109/TVCG.2024.3421555) 2
- [11] R. Fuchs, R. Peikert, H. Hauser, F. Sadlo, and P. Muigg. Parallel vectors criteria for unsteady flow vortices. *IEEE Transactions on Visualization and Computer Graphics*, 14(3):615–626, 2008. doi: [10.1109/TVCG.2007.70633](https://doi.org/10.1109/TVCG.2007.70633) 2
- [12] I. M. Gelfand and S. V. Fomin. *Calculus of variations*. Prentice-Hall Inc., Englewood Cliffs, N. J., 1963. doi: [10.1017/S0008439500032045](https://doi.org/10.1017/S0008439500032045) 5
- [13] A. Globus, C. Levit, and T. Lasinski. A tool for visualizing the topology of three-dimensional vector fields. In *Proc. Visualization'91*, pp. 33–40, 1991. doi: [10.1109/VISUAL.1991.175773](https://doi.org/10.1109/VISUAL.1991.175773) 2
- [14] T. Günther, M. Gross, and H. Theisel. Generic objective vortices for flow visualization. *ACM Transactions on Graphics (Proc. SIGGRAPH)*, 36(4):141:1–141:11, 2017. doi: [10.1145/3072959.3073684](https://doi.org/10.1145/3072959.3073684) 1, 2, 3, 4, 7, 8, 9
- [15] T. Günther, M. Schulze, and H. Theisel. Rotation invariant vortices for flow visualization. *IEEE Transactions on Visualization and Computer Graphics (Proc. IEEE Scientific Visualization)*, 22(1):817–826, 2015. doi: [10.1109/TVCG.2015.2467200](https://doi.org/10.1109/TVCG.2015.2467200) 2
- [16] T. Günther and H. Theisel. The state of the art in vortex extraction. *Computer Graphics Forum*, 37(6):149–173, 2018. doi: [10.1111/cgf.13319](https://doi.org/10.1111/cgf.13319) 1, 2
- [17] T. Günther and H. Theisel. Objective vortex corelines of finite-sized objects in fluid flows. *IEEE Transactions on Visualization and Computer Graphics (IEEE Visualization)*, 25(1):956–966, 2019. doi: [10.1109/TVCG.2018.2864828](https://doi.org/10.1109/TVCG.2018.2864828) 2
- [18] T. Günther and H. Theisel. Hyper-objective vortices. *IEEE Transactions on Visualization and Computer Graphics*, 26(3):1532–1547, 2020. doi: [10.1109/TVCG.2018.2868760](https://doi.org/10.1109/TVCG.2018.2868760) 2, 3, 7
- [19] T. Günther and H. Theisel. Objective Lagrangian vortex cores and their visual representations - demo, 2024. doi: [10.5281/zenodo.12750719](https://doi.org/10.5281/zenodo.12750719) 7
- [20] M. Hadwiger, M. Mlejnek, T. Theußl, and P. Rautek. Time-dependent flow seen through approximate observer Killing fields. *IEEE Transactions on Visualization and Computer Graphics*, 25(1):1257–1266, 2019. doi: [10.1109/TVCG.2018.2864839](https://doi.org/10.1109/TVCG.2018.2864839) 2, 3, 4, 5, 6, 8
- [21] G. Haller. An objective definition of a vortex. *Journal of fluid mechanics*, 525:1–26, 2005. doi: [10.1017/S0022112004002526](https://doi.org/10.1017/S0022112004002526) 2
- [22] G. Haller, A. Hadjighasem, M. Farazmand, and F. Huhn. Defining coherent vortices objectively from the vorticity. *Journal of Fluid Mechanics*, 795:136–173, 2016. doi: [10.1017/jfm.2016.151](https://doi.org/10.1017/jfm.2016.151) 2, 6
- [23] J. C. R. Hunt. Vorticity and vortex dynamics in complex turbulent flows. *Transactions on Canadian Society for Mechanical Engineering (Proc. CANCAM)*, 11(1):21–35, 1987. doi: [10.1139/tcsme-1987-0004](https://doi.org/10.1139/tcsme-1987-0004) 2
- [24] J. Jeong and F. Hussain. On the identification of a vortex. *Journal of Fluid Mechanics*, 285:69–94, 1995. doi: [10.1017/S0022112095000462](https://doi.org/10.1017/S0022112095000462) 2
- [25] B. Jobard and W. Lefer. Creating evenly-spaced streamlines of arbitrary density. In *Visualization in Scientific Computing '97*, pp. 43–55. Springer Vienna, Vienna, 1997. 7
- [26] B. Kaszás, T. Pedergrana, and G. Haller. The objective deformation component of a velocity field. *European Journal of Mechanics - B/Fluids*, 98:211–223, 2023. doi: [10.1016/j.euromechflu.2022.12.007](https://doi.org/10.1016/j.euromechflu.2022.12.007) 5
- [27] J. Kim, P. Moin, and R. Moser. Turbulence statistics in fully developed channel flow at low reynolds number. *Journal of fluid mechanics*, 177:133–166, 1987. doi: [10.1017/S0022112087000892](https://doi.org/10.1017/S0022112087000892) 2
- [28] J. Liu, Y. Gao, and C. Liu. An objective version of the vortex vector for vortex identification. *Physics of Fluids*, 31(6):065112, 2019. doi: [10.1063/1.5095624](https://doi.org/10.1063/1.5095624) 2
- [29] H. J. Lugt. The dilemma of defining a vortex. In *Recent developments in theoretical and experimental fluid mechanics*, pp. 309–321. Springer, 1979. doi: [10.1007/978-3-642-67220-0_32](https://doi.org/10.1007/978-3-642-67220-0_32) 2
- [30] R. Peikert and M. Roth. The "Parallel Vectors" operator – a vector field visualization primitive. In *Proc. IEEE Visualization*, pp. 263–270. IEEE, San Francisco, CA, USA, 1999. doi: [10.1109/VISUAL.1999.809896](https://doi.org/10.1109/VISUAL.1999.809896) 2, 3, 7
- [31] S. Popinet. Free computational fluid dynamics. *ClusterWorld*, 2(6):7, 2004. 7, 8
- [32] P. Rautek, M. Mlejnek, J. Beyer, J. Troidl, H. Pfister, T. Theußl, and M. Hadwiger. Objective observer-relative flow visualization in curved spaces for unsteady 2D geophysical flows. *IEEE Transactions on Visualization and Computer Graphics*, 27(2):283–293, 2020. doi: [10.1109/TVCG.2020.3030454](https://doi.org/10.1109/TVCG.2020.3030454) 2
- [33] P. Rautek, X. Zhang, B. Woschizka, T. Theußl, and M. Hadwiger. Vortex lens: Interactive vortex core line extraction using observed line integral convolution. *IEEE Transactions on Visualization and Computer Graphics (Proceedings IEEE VIS 2023)*, 30(1):55–65, 2024. doi: [10.1109/TVCG.2023.3326915](https://doi.org/10.1109/TVCG.2023.3326915) 1, 2, 3, 4, 7, 8, 9
- [34] S. K. Robinson. Coherent motions in the turbulent boundary layer. *Annual Review of Fluid Mechanics*, 23(1):601–639, 1991. doi: [10.1146/annurev.fl.23.010191.003125](https://doi.org/10.1146/annurev.fl.23.010191.003125) 2
- [35] M. Roth and R. Peikert. A higher-order method for finding vortex core lines. In *Proceedings Visualization '98 (Cat. No.98CB36276)*, pp. 143–150, 1998. doi: [10.1109/VISUAL.1998.745296](https://doi.org/10.1109/VISUAL.1998.745296) 2, 3, 7
- [36] J. Sahner, T. Weinkauff, N. Teuber, and H.-C. Hege. Vortex and strain skeletons in Eulerian and Lagrangian frames. *IEEE Transactions on Visualization and Computer Graphics*, 13:980–990, 10 2007. doi: [10.1109/TVCG.2007.1053](https://doi.org/10.1109/TVCG.2007.1053) 3, 7
- [37] D. Sujudi and R. Haimes. Identification of swirling flow in 3D vector fields. Technical report, Departement of Aeronautics and Astronautics, MIT, 1995. AIAA Paper 95-1715. doi: [10.2514/6.1995-1715](https://doi.org/10.2514/6.1995-1715) 2
- [38] C. Truesdell and W. Noll. *The nonlinear field theories of mechanics*. Handbuch der Physik, Band III/3, e by Flugge, S., (ed.), Springer-Verlag, Berlin, 1965. doi: [10.1007/978-3-662-10388-3_2](https://doi.org/10.1007/978-3-662-10388-3_2)
- [39] T. Weinkauff, J. Sahner, H. Theisel, and H.-C. Hege. Cores of swirling particle motion in unsteady flows. *IEEE Transactions on Visualization and Computer Graphics (Proc. Visualization)*, 13(6):1759–1766, 2007. doi: [10.1109/TVCG.2007.70545](https://doi.org/10.1109/TVCG.2007.70545) 2, 3, 7, 8
- [40] X. Zhang, M. Hadwiger, T. Theußl, and P. Rautek. Interactive exploration of physically-observable objective vortices in unsteady 2D flow. *IEEE Transactions on Visualization and Computer Graphics*, 28(1):281–290, 2022. doi: [10.1109/TVCG.2021.3115565](https://doi.org/10.1109/TVCG.2021.3115565) 2, 3
- [41] J. Zhou, R. J. Adrian, S. Balachandar, and T. Kendall. Mechanisms for generating coherent packets of hairpin vortices in channel flow. *Journal of fluid mechanics*, 387:353–396, 1999. doi: [10.1017/S002211209900467X](https://doi.org/10.1017/S002211209900467X) 2